

Cite this: *Soft Matter*, 2012, **8**, 995

www.rsc.org/softmatter

PAPER

# On the alignment of a cylindrical block copolymer: a time-resolved and 3-dimensional SFM study†

Clemens Liedel,<sup>a</sup> Markus Hund,<sup>b</sup> Violetta Olszowka<sup>b</sup> and Alexander Böker<sup>\*ac</sup>

Received 9th August 2011, Accepted 7th October 2011

DOI: 10.1039/c1sm06531a

In a combined quasi *in situ* scanning force microscopy study we close trace the alignment process of thin polymer films of poly(styrene)-*b*-poly(2-vinylpyridine)-*b*-poly(*tert*-butyl methacrylate) triblock terpolymer exposed to a high electric in-plane field and solvent vapor. Our experiments show that in this triblock terpolymer a perforated lamella structure forms the basis for the core-shell cylindrical structure. Further we observe a hexagonal superstructure during the alignment process that occurs with solvent vapor annealing in the presence of a high electric field (6–15 V  $\mu\text{m}^{-1}$ ). The electric field induced reorientation includes a rupture-and-growth mechanism and the rotation of the hexagonal lattice. We reconstruct the 3D-structure of the aligned microdomains with quasi *in situ* SFM nanotomography. The gained 3D reconstructions lead to a detailed understanding of the polymer film behavior in the border region between perforated lamella and the cylindrical phase. Combining time-resolved SFM datasets with 3D reconstructions, we present a model for the rearrangement of the polymer cylinders on the basis of a hexagonally perforated lamella. One-dimensionally aligned core-shell cylinders could form the basis for electrically isolated nanowires once the cylinder core is metalized.

## Introduction

Molecular self-assembly of block copolymers in thin films is a promising method for the structuring of surfaces on the nanometre scale. The obtained order is usually limited to microdomains in the size of some tens of nanometres. To obtain a macroscopic order or even a single domain structure, external fields can be applied to the polymer film.<sup>1,2</sup> Besides gradient fields (e.g. shear fields,<sup>3–5</sup> temperature gradients<sup>6–8</sup>), the use of electric fields for the alignment of block copolymer microdomains has been shown in the melt or in concentrated solutions.<sup>9–15</sup>

For the reorientation mechanism in block copolymer melt thin films, Amundson postulated two main orientation mechanisms: the movement and elimination of defects and the electric field induced selective disordering.<sup>16</sup> Nucleation and growth as well as grain rotation are dominant in concentrated block copolymer solutions exposed to a high electric field in bulk samples. In weakly phase separated systems, microdomains aligned parallel to the electric field vector grow at the expense of those aligned parallel to the electrodes. The rotation of unfavorably oriented

grains by defect movement usually occurs in highly phase separated block copolymer solutions.<sup>14</sup> In thin films of a block copolymer swollen in solvent vapor, rough alignment parallel to the electric field vector was achieved by rupture and reformation. Improvement of the order in a structure that is almost perfectly aligned parallel to the electric field lines proceeds *via* movement and annihilation of defects.<sup>10</sup> Still, in thin films also more complex alignment mechanisms can be observed. Olszowka observed that with successive E-field application of a lamella forming block copolymer, first ringlike defects (tori-defects) emerge while defect configurations with interrupted continuity of a lamella domain (open-end defects) are annihilated continuously.<sup>17</sup>

In a thin film of a cylinder forming diblock copolymer melt with film thickness equal to the cylinder spacing in the bulk, a perforated lamella (PL) phase is formed. Ly *et al.* have shown by dynamic density functional theory simulations that by applying an electric field, this PL transforms to cylinders. Here, the arms of 3-fold branching points that are not in the direction of the applied field vectors break. A transition state with insufficient annealing and/or E-field application results in a mixed morphology of PL and undulating cylinders.<sup>18</sup>

The alignment of cylinder forming polymers and its mechanism were studied using scattering methods and TEM cross-sections in thick films.<sup>19,20</sup> In thin films below one micrometre film thickness, mainly the final aligned structure was studied.<sup>9,21,22</sup> In simulations, spherical and bicontinuous intermediate structures were found during the alignment.<sup>23</sup> In experiments, a spherical intermediate was verified while aligning

<sup>a</sup>Lehrstuhl für Makromolekulare Materialien und Oberflächen, RWTH Aachen University and DWI an der RWTH Aachen e.V., 52056, Aachen, Germany. E-mail: boeker@dwi.rwth-aachen.de; Fax: +49 241 80 23301; Tel: +49 241 80 23304

<sup>b</sup>Physikalische Chemie II, Universität Bayreuth, 95440 Bayreuth, Germany  
<sup>c</sup>JARA-FIT, RWTH Aachen University, 52056, Aachen, Germany

† Electronic supplementary information (ESI) available: Details on the measurements and data processing/evaluation. See DOI: 10.1039/c1sm06531a

a  $\sim 500$  nm thick film.<sup>24</sup> Still, there is no detailed understanding of the alignment mechanisms on the scale of individual cylinders to date. Furthermore, core-shell structures have not yet been studied in E-Field alignment experiments to the best of our knowledge. For an overview on block copolymer structures in thin films in general, see ref. 25.

3D imaging of various types of sample materials can be carried out based on non-destructive or destructive techniques.<sup>26</sup> Non-damaging techniques are X-ray microscopy,<sup>27–31</sup> transmission electron microscopy (TEM),<sup>32–35</sup> atom probe field ion microscopy (APFIM),<sup>36</sup> and focused-ion-beam (FIB) tomography.<sup>37–40</sup> A recently published non-damaging depth-resolved imaging method is based on scanning force microscopy (SFM) and tip indentation mapping.<sup>41</sup> Destructive methods are based on measuring ultra-thin layers of the sample material *e.g.* by combining the ultramicrotome technique with scanning force microscopy (SFM)<sup>42</sup> or with scanning electron microscopy (SEM).<sup>43</sup>

Using common *in situ* methods that are based on electron microscopy like TEM or scanning electron microscopy (SEM) imaging combined with plasma etching, sensitive surfaces like polymer materials can be easily destroyed by the electron beam.<sup>44,45</sup> The combination of ultramicrotoming with SFM is limited to a step-size of at least 20 nm due to the ultramicrotome setup.<sup>42</sup> The depth range of the SP-based method by Spitzner *et al.* is limited by the tip indentation (material dependent by the compliance of the material).<sup>41</sup>

In contrast to the above mentioned techniques, with nanotomography as a SPM-based method, material properties can be mapped in 3D volume space. It combines well-established SPM surface characterization with suitable ablation techniques. Various SPM techniques and erosion methods like plasma etching, chemical wet etching or mechanical polishing can be combined.<sup>46–48</sup>

The successive erosion of thin specimen layers followed by scanning each newly exposed surface leads to a series of topography and corresponding property maps which can be combined to a real space volume image of the sample. Performing nanotomography with a scanning force microscope (SFM), both the topography and the corresponding material maps are accessible using standard SFM modes like tapping-mode imaging. For example, the second flexural eigenmode of the cantilever can be used for phase imaging combined with wet chemical etching as the ablation method.<sup>49,50</sup> Other techniques like HarmoniX<sup>TM51,52</sup> or Peakforce QNM<sup>TM53</sup> could also be used to perform nanotomography.

A suitable ablation method for sensitive polymer materials is low pressure (LP) plasma treatment. By adjusting process parameters like gas composition, process pressure, treatment time, and rf power, thin layers in the low nanometre regime can be removed in a precise and reproducible way without creating noteworthy thermal load or mechanical stress to the specimen.<sup>54,55</sup> For a poly(styrene)-*b*-poly(2-vinylpyridine)-*b*-poly(*tert*-butyl methacrylate) triblock (SVT) copolymer material like the one described in this paper, low pressure plasma was already successfully used for etching.<sup>56</sup> Generally, the type of etching technique can be regarded as a key enabling technique for a successful nanotomographic examination, because it limits its practical application as a matter of principle, and more

specifically, the accomplishable depth-resolution, quality and quantity of the acquired data.

In the setups described by Magerle<sup>48</sup> and Konrad *et al.*<sup>47</sup> plasma etching is performed *ex situ* in a system separated from the SFM. This leads to time-consuming measurement protocols for relocating the same sample spot and results in general low performance. Moreover it leads to principle problems of practicability and manageability. Known recipes to relocate to a specific sample spot are based on landmarks on the sample surface. They fail if the landmark vanishes or changes its shape due to the treatment effects. Moreover, taking large overview images in order to reposition the probe relative to the sample results in “stress” to the probe and hence reduced image quality. In order to overcome these problems and principle limitations of common *in situ* techniques, Hund *et al.* developed a quasi *in situ* scanning probe microscope which enables even harsh sample treatments like LP-plasma, solvent vapor treatments under high electric fields<sup>10,17,57</sup> and other aggressive treatments inside the SFM which are normally not possible to apply while scanning like harsh chemical treatments.<sup>58–60</sup> During sample treatment the probe is therefore spatially separated from the sample. After each SPM characterization, the probe is macroscopically separated from the sample surface while the sample is stationary (see “lock mode”, ref. 59, p. 3). Hence, high position stability (sample/probe) is reached.

The quasi *in situ* SFM setups used in this paper to study the alignment of SVT polymer microdomains and to perform the nanotomographic examination utilize modified commercial SFMs (Dimension<sup>TM</sup> 3100 series from Veeco Instruments, Inc.) and specific process equipment. For solvent vapor annealing in the presence of a high electric field, the system is equipped with an automatically operated reaction chamber featuring automated opening, closing, and an active sealing. It turned out that for our sample treatments (flow-through) a hermetically sealed chamber is mandatory for successful and reproducible treatment steps. The details of the PC-controlled reaction chamber and a fully automated QIS-SFM system featuring a synchronization of data acquisition and sample treatment steps (including sample spot tracking) are described elsewhere.<sup>61</sup>

The outline of the paper is as follows: first we present the typical structures of poly(styrene)-*b*-poly(2-vinylpyridine)-*b*-poly(*tert*-butyl methacrylate) triblock terpolymer (SVT) before and after annealing in an electric field and solvent vapor (SEM images). We compare the results with nanotomographic reconstructions of the aligned SVT. To investigate the alignment mechanism, we discuss results of time-resolved quasi *in situ* SFM data. Finally, we suggest an alignment model with cylinders based on a perforated lamella structure.

## Experimental

### Polymer

The studied cylinder forming ABC triblock terpolymer consists of 16 wt% polystyrene (PS), 21 wt% poly(2-vinylpyridine) (P2VP) and 63 wt% poly(*tert*-butyl methacrylate) (PtBMA) with a total weight-average molecular weight  $M_w = 140 \text{ kg mol}^{-1}$  (denoted as  $S_{16}V_{21}T_{63}^{140}$ ; subscripts denote the weight percentage of the respective block while the superscript names the weight-average

molar mass in  $\text{kg mol}^{-1}$ ). The polymer was synthesized by sequential living anionic polymerization as described elsewhere.<sup>62</sup> Gel permeation chromatography of the block terpolymer yields a polydispersity of  $M_w/M_n = 1.03$ . In the bulk, the material has a structure of hexagonally packed core-shell cylinders embedded within the *PtBMA* matrix material. The characteristic spacing for  $S_{16}V_{21}T_{63}^{140}$  cylinders is  $71 \pm 3$  nm in the bulk (from SAXS measurements) and  $66 \pm 3$  nm in thin films (from SFM measurements).

### Polymer films

Films with a thickness of  $67 \pm 2$  nm were spin cast from chloroform solutions onto glass substrates, ensuring that only one cylindrical layer is found in the films. These films were pre-annealed in saturated  $\text{CHCl}_3$  vapor at room temperature for 9.5 min resulting in the starting cylinder morphology for our experiments. The structure consists, according to previous studies, of a thin brush layer where the P2VP block is attached to the surface.<sup>63</sup> Above this brush layer, core-shell-structures of PS (core) and P2VP (shell) are embedded in a matrix of *PtBMA*. The latter is aligned at the free surface because of the lowest surface energy.<sup>64</sup>

### Substrates

For our experiments, we used glass substrates with evaporated gold electrodes of 28 nm height.<sup>65</sup> The electrode distance was chosen as one specific value between 5 and 10 microns. The very large aspect ratio between electrode spacing and the electrode length (6 mm) allows applying a homogeneous electric field.<sup>66</sup>

### SEM

SEM images were taken using a Zeiss Leo Gemini instrument with a field emission cathode at a voltage of 0.5 kV. By the exposure to an electron beam in the SEM, the *PtBMA* block within the  $S_{16}V_{21}T_{63}^{140}$  was depolymerized and evaporated. As this block builds the matrix surrounding the PS-P2VP-core-shell-structures, matrix areas appear black in SEM images. No further staining of the films was necessary. From the order parameter derived from SEM measurements using gradient fields (the same technique like in ref. 65; not shown here), critical electric field strength for aligning the structures was derived as  $4.1 \text{ V } \mu\text{m}^{-1}$ . To be sure an optimal alignment is reached during the annealing time; the experiments described in this paper were performed well above that critical value at  $15 \text{ V } \mu\text{m}^{-1}$  unless mentioned otherwise.

### QIS-SFM

The quasi *in situ* setups utilize modified commercial Dimension™ 3100 SFMs (all from Veeco Instruments Inc.). They are equipped with a NanoScope® V controller and an XYZ closed-loop scanner (annealing experiments) and a NanoScope® IV controller and an XY closed-loop scanner (nanotomographic experiments), respectively. For both, the original sample chuck was replaced by a special air bearing table holding a specific reactor chamber module.

For solvent vapor annealing in the presence of a high electric field the system is equipped with an automatic operated reaction chamber featuring automated opening, closing, and an active sealing of the cover against the reactor chamber. It turned out that for our sample treatments (flow-through), a hermetically sealed chamber is mandatory for successful and reproducible treatment steps. The details of the PC-controlled reaction chamber and a fully automated QIS-SFM system featuring a synchronization of data acquisition and sample treatment steps (including sample spot tracking) are described elsewhere.<sup>61</sup>

For the nanotomographic experiments a plasma generation module (inductively coupled plasma source) was additionally installed. The system features an automatic tip/sample separation (movements of the *z*-stage in the mm range) with the help of a self-developed NanoScript™ application. Moreover, an automatic and triggered grounding of the sample during scanning was implemented. A detailed description of the setup is given elsewhere.<sup>58–60</sup> The experiments were performed using  $\text{Si}_3\text{N}_4$  cantilevers from Olympus (spring constant  $35\text{--}60 \text{ N m}^{-1}$ ; resonance frequency  $280\text{--}340 \text{ kHz}$ ).

The scan area ( $3 \mu\text{m} \times 3 \mu\text{m}$ ) was kept constant during the experiment. In a first post-processing step the remaining lateral offsets between successive SFM images were corrected by maximization of the cross-correlation between the images. We note that the used SFM is equipped with a state-of-the-art closed-loop scanner, which drastically reduces image distortions.

After registration, a smaller detail of each SFM image was cut out to provide a series of images taken at exactly the same spot of the sample. Further details on the measurements and data processing/evaluation can be found in the ESI†.

## Results

For our studies we use a poly(styrene)-*b*-poly(2-vinylpyridine)-*b*-poly(*tert*-butyl methacrylate) triblock terpolymer, further denoted as  $S_{16}V_{21}T_{63}^{140}$ , like described previously.<sup>56,62,63,67,68</sup> The subscript denotes the weight percentage of each component, and the superscript gives the overall molecular weight in  $\text{kg mol}^{-1}$ . Core-shell cylinders and hexagonally perforated core-shell lamellae of polystyrene (PS, core) and poly(2-vinylpyridine) (P2VP, shell) in a poly(*tert*-butyl methacrylate) (*PtBMA*) matrix were observed in thin films. The matrix covers the PS-P2VP structures. After spin-coating of a  $S_{16}V_{21}T_{63}^{140}$  film from chloroform solution onto silicon or glass, the structure equilibrated after 9.5 min of chloroform vapor annealing. The interaction parameters  $\chi$  between the individual homopolymer blocks and the solvent are  $\chi_{\text{PS/CHCl}_3} = 0.35$ ,  $\chi_{\text{P2VP/CHCl}_3} = 0.38$  and  $\chi_{\text{PtBMA/CHCl}_3} = 0.40$  like derived from the Hildebrand solubility parameters.<sup>69</sup> As they do not deviate much from each other, the solvent is nearly unselective. For further details, see ESI†. In topographic SFM images (see Fig. S1, ESI†) a mainly striped pattern is found.

Fig. 1a shows a SEM image of a  $S_{16}V_{21}T_{63}^{140}$  polymer film after 9.5 min chloroform annealing in which the top covering layer was removed (depolymerized and vaporized by the electron beam). Dark lines and spots can be observed between the gray areas.

Fig. 1b shows the polymer film after additional annealing in pure chloroform vapor in the presence of an electric field ( $6 \text{ V}$

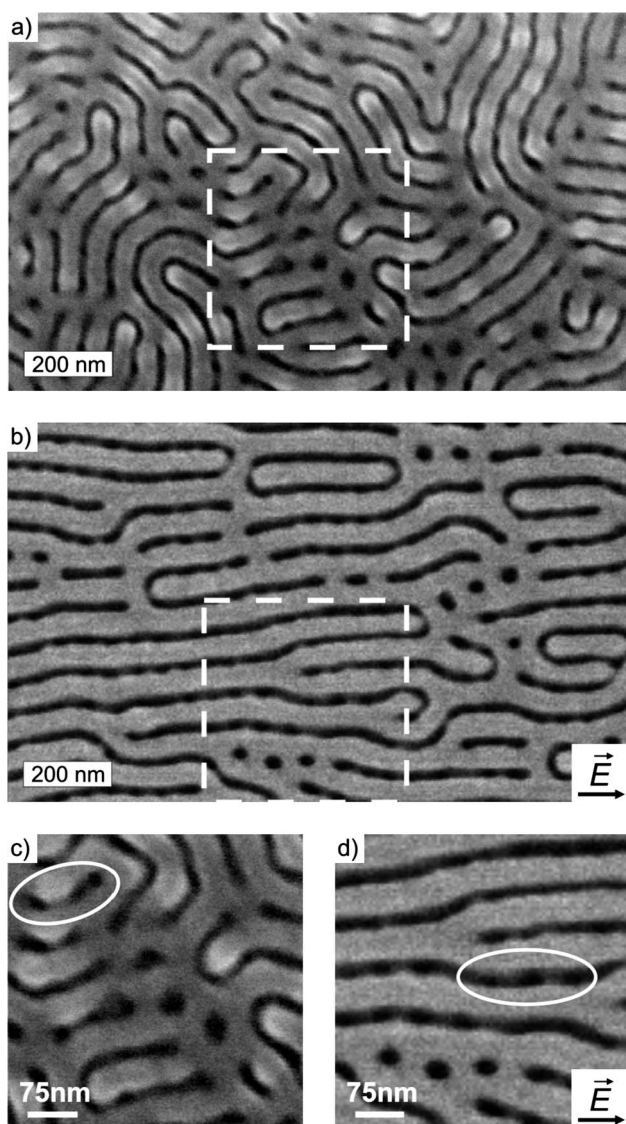


**Fig. 1** SEM images of a  $S_{16}V_{21}T_{63}^{140}$  polymer film. (a) After annealing for 9.5 min in saturated chloroform vapor; (b) after additional 5 h annealing in saturated chloroform vapor in the presence of an electric field ( $6 \text{ V } \mu\text{m}^{-1}$ , electric field vector direction is horizontal); (c) and (d) are the corresponding cutouts (*cf.* dashed areas in (a) and (b)). The indicated brighter and darker spots are hints to bridging areas. (a) and (b) are not taken at the same sample spot.

$\mu\text{m}^{-1}$ , 5 h) at a different sample spot. Fig. 1c and d show corresponding cutouts (*cf.* dashed white areas in Fig. 1a and b). Dark spots and dark lines (Fig. 1c) which are aligned preferentially in the direction of the electric field vector (Fig. 1d) are clearly visible.

Because the *Pt*BMA block in  $S_{16}V_{21}T_{63}^{140}$  polymer was destroyed by the electron beam,<sup>32</sup> we assign the dark areas to the matrix material. The remaining gray areas hence consist of a mixed phase of PS–P2VP cylinders and perforated lamellae. Before and after the annealing, PL clusters appear in the cylindrical surface structure. The dark lines between the cylinders contain brighter and darker spots that hint to bridging areas between the cylinder forming polymer blocks (marked by white ellipses in Fig. 1c and d).

To verify the composition of these bridges, we perform quasi *in situ* scanning force microscopy (QIS-SFM) nanotomography using low pressure plasma treatments (22 etching steps) of a  $S_{16}V_{21}T_{63}^{140}$  film aligned using an in-plane electric field ( $15 \text{ V } \mu\text{m}^{-1}$ , 5 h chloroform annealing, for details see Experimental section and ESI†).

The covering matrix of *Pt*BMA can be easily removed<sup>63</sup> because the *tert*-butyl group is very sensitive with respect to LP-plasma. Upon subsequent low pressure plasma treatments the weak ester linkages break and small species are vaporized.<sup>70</sup>

Fig. 2 shows 3D reconstructions of a  $S_{16}V_{21}T_{63}^{140}$  polymer film sample at two spots. The topographic and the corresponding phase information (tapping-mode imaging, raw data  $3 \mu\text{m} \times 3 \mu\text{m}$ ) are combined to 3D volume datasets. Red parts correspond to the core–shell structures while the matrix appears transparent. Because of the similar properties and because the PS phase is surrounded by P2VP it is not possible to distinguish the PS and P2VP phases while we can clearly discern the cylinders from the matrix. For a detailed explanation of the used data evaluation including the voxelization algorithm and the *z*-calibration, see the Experimental section, ref. 60 and ESI†.

In Fig. 2a, a regular network of nearly perfectly aligned cylinders is shown (arrows indicate direction of the electric field vector). In Fig. 2b PL domains can be clearly observed (marked by a yellow dashed ellipse). At some spots (examples marked by white circles) undulating cylinders are approaching each other or connect *via* thin bridges to form a PL structure. The matrix polymer between these cylinders forms perforations that are either spot-like or are formed by the connection of neighboring spots. This finding of spot-like and connected linear elongated perforations is very similar to the theoretical predictions of Ly *et al.*<sup>18</sup> in which a HPL structure transforms to an aligned cylindrical one by applying an electric field in the lamellar plane.

These findings let us assume that an underlying perforated lamella structure forms the basis for the cylindrical structure here. This is supported by viewing the PL as parallel cylinders ( $C_{\parallel}$ ) containing a regular network of 3-fold branching points which are structural defects in the  $C_{\parallel}$  phase. Through an undulating film thickness, the PL can emerge out of a cylindrical phase in ABA triblock terpolymer thin films.<sup>71,72</sup> The SEM images in Fig. 1 and the previously observed hexagonally perforated lamella in this polymer<sup>56,62,63,67,68</sup> confirm this assumption. Because of the structural similarity of the PL and  $C_{\parallel}$  phases and as there seems to be an equilibrium between cylinders and perforated lamellae or a perforated superstructure, we further refer to the general term core–shell structures even though we only talk about core–shell cylinders and perforated core–shell lamellae.

In order to study the process of orientation that leads to the aligned structures (Fig. 1 and 2), we performed QIS-SFM experiments with an applied electric field of  $15 \text{ V } \mu\text{m}^{-1}$  in the presence of chloroform vapor. It is important to mention that cylindrical and perforated structures under the covering *Pt*BMA matrix can be observed in SFM topographic images after solvent annealing because of the slightly different drying rates of the blocks from solution.<sup>73</sup>

Fig. 3 shows the evolution of the pre-annealed structure (Fig. 3a) to an aligned structure (Fig. 3e) of a  $S_{16}V_{21}T_{63}^{140}$  polymer thin film as a function of cumulative treatment time in

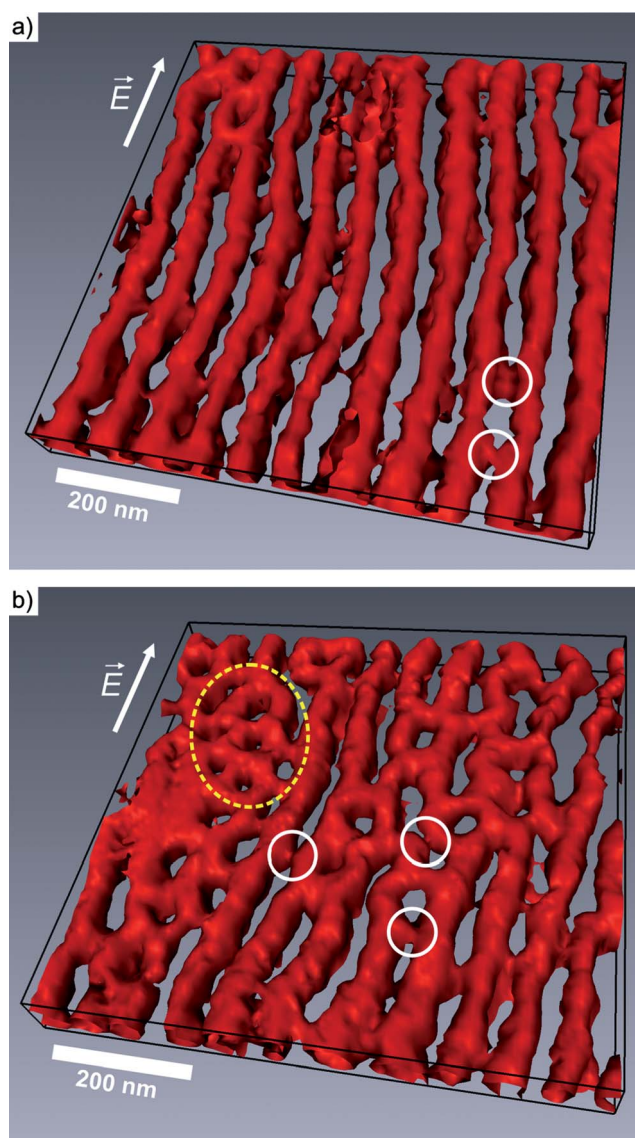


**Fig. 2** 3D reconstruction of a  $S_{16}V_{21}T_{63}^{140}$  polymer film treated with chloroform vapor annealing in the presence of an in-plane electric field of  $15 \text{ V } \mu\text{m}^{-1}$  for 5 h. Two different spots of the same sample are shown: (a) core-shell structures (red) and matrix material P7BMA (transparent) ( $300 \times 300 \times 31$  voxels); (b) mixed cylindrical and perforated lamella (yellow dashed circle) morphology ( $300 \times 300 \times 32$  voxels). Nanotomographic volume images displayed as isosurface. Cylinders are aligned parallel to the electric field vector. Thin bridging areas (examples are shown in white circles) between two cylinders are highlighted (white circles).

the presence of an electric field ( $15 \text{ V } \mu\text{m}^{-1}$ ). 14 SFM images have been taken at a specific sample spot, five of which are exemplified in Fig. 3 (topography). According to previous studies<sup>56,67</sup> we can relate the darker (lower) structures in the SFM topographic images of the quenched films to the core-shell structures. The brighter (higher) parts correspond to the P7BMA-filled perforations. The starting structure was a pre-annealed polymer film (9.5 min in saturated chloroform vapor without electric field). For the experiments, a grain with structures initially oriented normal to the electric field vector was chosen (Fig. 3a). The time “0 min” expresses that no E-field has been applied before. In the intermediate time-range (Fig. 3b–d), the normal orientation

breaks at the expense of the parallel one. Even with studying the bright areas in SFM topographic images, which correspond to the matrix between the cylinders and in the perforations, the orientation of the cylindrical structures (darker areas in SFM images) becomes visible as each cylinder is situated between two elongated perforations (bright lines).

After 11 minutes of E-field and solvent vapor annealing (Fig. 3e), the predominant orientation develops parallel to the electric field vector. Because of resolution issues (due to a fast dewetting of the film), in the following experiments, we use 67% saturated chloroform vapor to anneal the film (Fig. 4). After 6 min of treatment (E-field strength of  $15 \text{ V } \mu\text{m}^{-1}$  and solvent vapor) a bright line that is aslant to the electric field vector is visible in the center of the image (a), highlighted with white ellipse. With further annealing, the angle between this line and the electric field vector decreases continuously (Fig. 4b and c). After 49.5 min of annealing under an electric field, the bright line is oriented parallel to the electric field vector (Fig. 4d). As mentioned, the bright areas correspond to the P7BMA matrix filling the perforations in every layer of cylinders. As the elongated perforations rotate, cylinders situated next to the bright lines in SFM images align by some rotation mechanism as well.

## Discussion

### Perforated superstructure

In the following we propose an alignment mechanism of  $S_{16}V_{21}T_{63}^{140}$  polymer films exposed to in-plane electric fields. Like recently simulated in the group of Zvelindovsky,<sup>18,72</sup> the electric field induced transition from a perforated to a cylindrical structure in AB and ABA block copolymers proceeds through the combination of adjacent perforations. During the transition, the newly formed cylinders contain undulations resulting from former matrix branching points.

In a cylinder forming block copolymer,  $-1/2$  disclinations can contain PL clusters that are metastable.<sup>74</sup> By solvent vapor annealing of such a film in the absence of an electric field, perforated lamella defects have lifetimes ranging from minutes to hours<sup>75</sup> and can also appear as nuclei for the formation of stable PL grains.<sup>76,77</sup> One polymer can establish stable PL and  $C_{\parallel}$  phases depending on the film thickness without a change of the surface fields.<sup>72</sup>

Fig. 1 and 2 show a mixed morphology of PL and  $C_{\parallel}$  in  $S_{16}V_{21}T_{63}^{140}$  polymer thin films before and after applying an electric field. Same as after solvent vapor annealing with no electric field applied, PL domains are apparently stable in the cylindrical phase. Undulations in the cylindrical domains also point to a tendency to form PL domains. This supports the assumption of a perforated superstructure. In Fig. 5, white lines connect the darkest spots in the SEM images from Fig. 1 before and after extensive annealing (a and b, respectively). A mainly hexagonal arrangement of the dark spots becomes obvious. Yellow and blue circles denote exceptions from the hexagonal arrangement. Here, perforations are arranged either in a pentagonal (yellow) or heptagonal (blue) shape. In a hexagonal lattice, such  $5/7$  defects are well known.<sup>78</sup> They appear preferentially in the close vicinity to structural defects like disclinations and dislocations. The hexagonal superstructure for the polymer

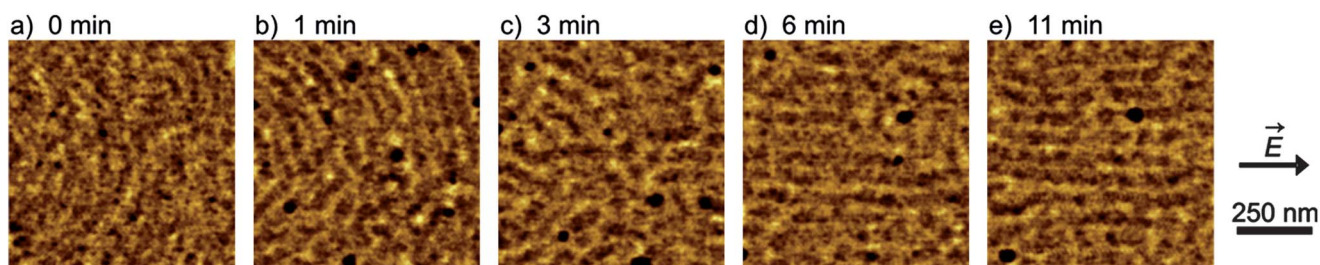


**Fig. 3** Alignment of microdomains of a  $S_{16}V_{21}T_{63}^{140}$  polymer film. Series of registered QIS-SFM topographic images ( $750 \text{ nm} \times 750 \text{ nm}$ ) undergoing chloroform vapor annealing (100% saturated using argon) in the presence of an electric field of  $15 \text{ V } \mu\text{m}^{-1}$ . (a) Pre-annealed sample (9.5 min without electric field); (b–e) cumulative electric field treatment time as indicated.

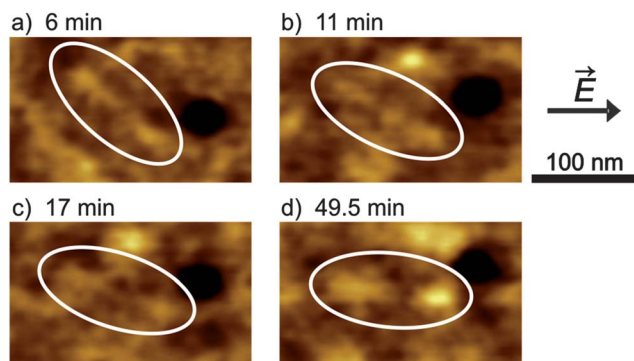


**Fig. 4** Series of QIS-SFM topographic images of a  $S_{16}V_{21}T_{63}^{140}$  polymer film ( $15 \text{ V } \mu\text{m}^{-1}$  and 67% saturated chloroform vapor in argon;  $234 \text{ nm} \times 141 \text{ nm}$ ). Alignment of the highlighted structure to the direction of the E-field vector. Cumulative treatment times as indicated.

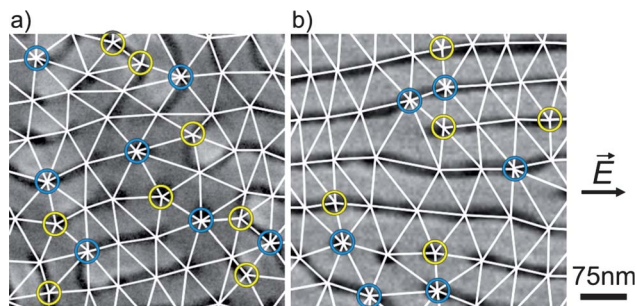


**Fig. 5** SEM images of a  $S_{16}V_{21}T_{63}^{140}$  polymer film (same as Fig. 1c and d). (a) After annealing for 9.5 min in saturated chloroform vapor; (b) after additional 5 h annealing in saturated chloroform vapor with an applied electric field of  $6 \text{ V } \mu\text{m}^{-1}$ . The electric field vector runs in the horizontal direction. The images represent an area of  $450 \text{ nm} \times 450 \text{ nm}$ . White lines connect the black spots in the images. Most intersections are connected to six other ones forming a hexagonal lattice. Exceptions (where a junction is connected to five or seven other junctions) are marked by yellow or blue circles, respectively.

film is also supported by the appearance of the PL phase. Our results for  $S_{16}V_{21}T_{63}^{140}$  polymer thin films agree with similar calculations in ABA block copolymer thin films, where under certain parameters PL and  $C_{\parallel}$  domains coexist in a sample.<sup>79</sup> This indicates a strong structural similarity and can be interpreted as the PS–P2VP cylinders are arranged in a pattern formed by the PL structure. Without electric field, there is no preferred direction in the structure (Fig. 5a). After extended application of an

electric field (Fig. 5b), one of the three main directions of the surface lattice is nearly parallel to the electric field vector.

#### Alignment model

$S_{16}V_{21}T_{63}^{140}$  polymer cylinder alignment parallel to the electric field vector proceeds through two main mechanisms: rupture-and-reformation of cylinders (Fig. 3) and cylinder rotation (Fig. 4). The time scales of Fig. 3 and 4 are hardly comparable due to the different annealing conditions (67% vs. saturated chloroform vapor). In concentrated block copolymer solutions, Schmidt *et al.*<sup>80</sup> showed experimentally and theoretically that solutions with the initial block copolymer orientation normal to the electric field vector preferentially reorient by the nucleation-and-growth mechanism. Grain rotation by defect movement and annihilation is preferred if the initial orientation is aslant to the direction of the electric field vector. Keeping in mind the assumption of a hexagonally perforated lamella as the superstructure of aligned and non-aligned  $S_{16}V_{21}T_{63}^{140}$  core-shell cylinders (Fig. 5) and the different observed orientation mechanisms in Fig. 3 and 4, we present a model of the rearrangement of the cylinders with underlying perforated structure. This is schematically shown in Fig. 6. We assume that effects similar to the ones in concentrated solutions occur simultaneously. In the schematic 5/7 defects and their annihilation are not taken into account.

In Fig. 6a we show a perfect hexagonal arrangement of dark spots with most of them being connected randomly by black and red lines. The white area between these lines represents the cylinders of  $S_{16}V_{21}T_{63}^{140}$  while the black and red parts denote the

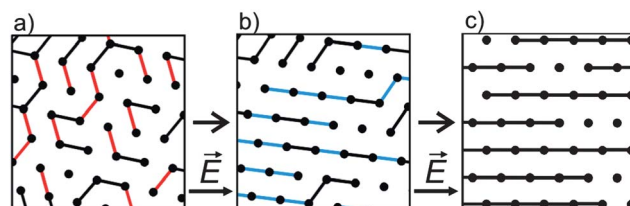


**Fig. 6** Model for the reorientation processes in a disordered cylindrical structure with a hexagonal perforated lamella superstructure exposed to an electric field. Black, red and blue lines and black spots represent the P<sub>1</sub>BMA matrix; the white area represents the cylindrical and perforated lamella PS–P2VP structures. (a–c) Two effects are shown simultaneously: rupture-and-reformation of red drawn matrix parts to form blue ones and the rotation of the hexagonal lattice.

PtBMA-filled perforations between the cylinders. The figure shows a similar structure to the one depicted in Fig. 1c and 5a before E-field application. After inducing mobility (solvent vapor) and a directing force (electric field) to the sample, the structures start to align in a preferred direction. The inter-cylindrical PtBMA areas that are oriented nearly normal to the electric field vector break and reform in nearby positions where they are almost parallel to the electric field vector, keeping the hexagonal lattice. Simultaneously, the lattice starts to rotate. Additionally, defects in the hexagonal structure might be annihilated (not shown here). A more detailed characterization of defect behavior is beyond the scope of this paper and is subject to further research. In Fig. 6b, blue lines show the PtBMA parts newly formed from the red drawn matrix parts in Fig. 6a. With further annealing in the presence of an electric field, lattice rotation and rupture processes continue to form the final aligned structure shown in Fig. 6c. In this figure, every cylinder is oriented parallel to the electric field vector. Like before the application of an electric field and solvent vapor, some PL domains persist. The structure is similar to the one shown in Fig. 1d and 5b.

### Hexagonal structure during solvent vapor annealing with applied electric field

To prove the existence of a hexagonal structure during solvent vapor annealing, we show QIS-SFM topographic images of a specific surface spot after 34.5 (a) and 49.5 (b) min annealing in the presence of an electric field (Fig. 7). The SFM images are treated in a similar way as the SEM-images of Fig. 5, *i.e.* we

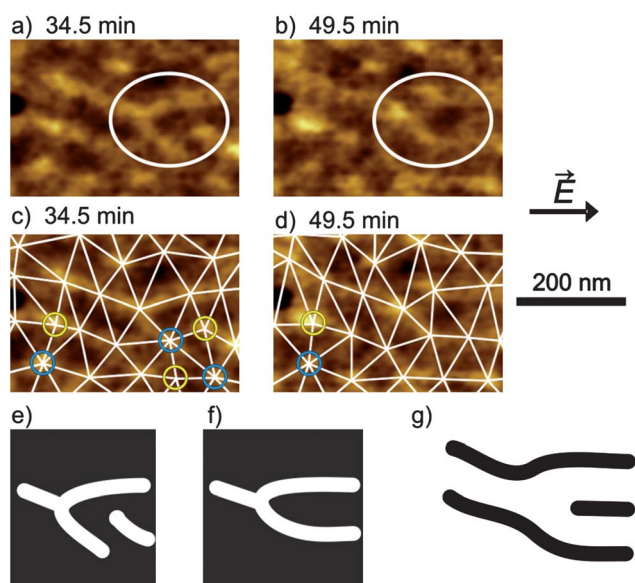


**Fig. 7** Series of registered QIS-SFM topographic images of a  $S_{16}V_{21}T_{63}^{140}$  polymer film during the application of an electric field ( $15 \text{ V } \mu\text{m}^{-1}$ ) and chloroform vapor (67% saturated in Ar) annealing ( $422 \text{ nm} \times 258 \text{ nm}$ ). Annihilation of the white marked  $+1/2$  matrix disclination and  $5/7$  perforated lamella defects. (a and c) After 34.5 min annealing; (b and d) after 49.5 min annealing; (c and d) mainly hexagonal arrangement of the brightest spots in (a) and (b); (e–g) sketches showing the defects in (a) and (b) (cylinders black, matrix white):  $+1/2$  matrix disclination before (e) and after healing (f) and cylinder dislocation (g).

connect the PtBMA domains (here: brightest spots) in Fig. 7a and b. This is shown in Fig. 7c and d, respectively. Like in Fig. 5 (before and after annealing in the presence of an electric field) this results in a mainly hexagonal arrangement with exceptions shown by yellow and blue circles after different times of E-field treatment. The finding of a hexagonal structure before, during and after annealing supports the model presented in Fig. 6.

In Fig. 7, we additionally observe defect annihilation. A cylinder dislocation combined with a  $+1/2$  matrix disclination (Fig. 7e; for structural defects in cylindrical block copolymer phases see Horvat *et al.*<sup>74</sup>) is visible in Fig. 7a and c. In Fig. 7b and d, the  $+1/2$  matrix disclination is annihilated due to rupture and reformation of a PS–P2VP cylinder (schematically shown in Fig. 7f). This also leads to annihilation of  $5/7$  perforated lamella defects (yellow and blue circles) in the hexagonal lattice. The cylinder dislocation persists (Fig. 7g).

### Conclusions

In this study, we extensively used the quasi *in situ* technique for both the time-resolved examination of a cylindrical block copolymer and the nanotomographic characterization of the gained structure. It turned out that the quasi *in situ* SFM technique presented in this study is very powerful and has a large potential which goes significantly beyond the problems studied here. The possibility of imaging the same spot of the sample allows to closely follow any sample changes occurring as a consequence of certain treatments, which may require a hermetically sealed reactor chamber and/or which cannot be applied in the presence of the tip. This may involve LP-plasma treatments as well as the exposure to solvent vapors in the presence of high electric fields as shown in the paper or other treatments *e.g.* aggressive chemicals and high electromagnetic fields.

### Acknowledgements

We thank Andrei V. Zvelindovsky for fruitful discussions and Andreas Fery and Larisa Tsarkova for support. Financial support by the Deutsche Forschungsgemeinschaft (DFG) and the European Union in the framework of the ERA-NanoSci+ project MEMORY is gratefully acknowledged. Clemens Liedel thanks the ENB Macromolecular Science and acknowledges the Fonds der Chemischen Industrie for financial support by a Chemiefonds Fellowship.

### Notes and references

- S. O. Kim, H. H. Solak, M. P. Stoykovich, N. J. Ferrier, J. J. de Pablo and P. F. Nealey, *Nature*, 2003, **424**, 411–414.
- L. Rockford, Y. Liu, P. Mansky, T. P. Russell, M. Yoon and S. G. J. Mochrie, *Phys. Rev. Lett.*, 1999, **82**, 2602–2605.
- R. J. Albalak and E. L. Thomas, *J. Polym. Sci., Part B: Polym. Phys.*, 1993, **31**, 37–46.
- D. E. Angelescu, J. H. Waller, D. H. Adamson, P. Deshpande, S. Y. Chou, R. A. Register and P. M. Chaikin, *Adv. Mater.*, 2004, **16**, 1736–1740.
- M. Kimura, M. J. Misner, T. Xu, S. H. Kim and T. P. Russell, *Langmuir*, 2003, **19**, 9910–9913.
- T. Hashimoto, J. Bodycomb, Y. Funaki and K. Kimishima, *Macromolecules*, 1999, **32**, 952–954.
- K. Mita, H. Tanaka, K. Saijo, M. Takenaka and T. Hashimoto, *Macromolecules*, 2007, **40**, 5923–5933.

- 8 K. Mita, H. Tanaka, K. Saijo, M. Takenaka and T. Hashimoto, *Macromolecules*, 2008, **41**, 6780–6786.
- 9 T. L. Morkved, M. Lu, A. M. Urbas, E. E. Ehrichs, H. M. Jaeger, P. Mansky and T. P. Russell, *Science*, 1996, **273**, 931–933.
- 10 V. Olszowka, M. Hund, V. Kuntermann, S. Scherdel, L. Tsarkova, A. Böker and G. Krausch, *Soft Matter*, 2006, **2**, 1089–1094.
- 11 T. Thurn-Albrecht, J. Schotter, G. A. Kastle, N. Emley, T. Shibauchi, L. Krusin-Elbaum, K. Guarini, C. T. Black, M. T. Tuominen and T. P. Russell, *Science*, 2000, **290**, 2126–2129.
- 12 K. Amundson, E. Helfand, D. D. Davis, X. Quan, S. S. Patel and S. D. Smith, *Macromolecules*, 1991, **24**, 6546–6548.
- 13 K. Amundson, E. Helfand, X. Quan and S. D. Smith, *Macromolecules*, 1993, **26**, 2698–2703.
- 14 A. Böker, H. Elbs, H. Hänsel, A. Knoll, S. Ludwigs, H. Zettl, V. Urban, V. Abetz, A. H. E. Müller and G. Krausch, *Phys. Rev. Lett.*, 2002, **89**, 135502.
- 15 A. Böker, A. Knoll, H. Elbs, V. Abetz, A. H. E. Müller and G. Krausch, *Macromolecules*, 2002, **35**, 1319–1325.
- 16 K. Amundson, E. Helfand, X. Quan, S. D. Hudson and S. D. Smith, *Macromolecules*, 1994, **27**, 6559–6570.
- 17 V. Olszowka, M. Hund, V. Kuntermann, S. Scherdel, L. Tsarkova and A. Böker, *ACS Nano*, 2009, **3**, 1091–1096.
- 18 D. Q. Ly, T. Honda, T. Kawakatsu and A. V. Zvelindovsky, *Macromolecules*, 2008, **41**, 4501–4505.
- 19 T. Thurn-Albrecht, J. DeRouchey, T. P. Russell and H. M. Jaeger, *Macromolecules*, 2000, **33**, 3250–3253.
- 20 T. Thurn-Albrecht, J. DeRouchey, T. P. Russell and R. Kolb, *Macromolecules*, 2002, **35**, 8106–8110.
- 21 P. Mansky, J. DeRouchey, T. P. Russell, J. Mays, M. Pitsikalis, T. Morkved and H. Jaeger, *Macromolecules*, 1998, **31**, 4399–4401.
- 22 T. Thurn-Albrecht, R. Steiner, J. DeRouchey, C. M. Stafford, E. Huang, M. Bal, M. Tuominen, C. J. Hawker and T. Russell, *Adv. Mater.*, 2000, **12**, 787–791.
- 23 K. S. Lyakhova, A. V. Zvelindovsky and G. J. A. Sevink, *Macromolecules*, 2006, **39**, 3024–3037.
- 24 T. Xu, A. V. Zvelindovsky, G. J. A. Sevink, K. S. Lyakhova, H. Jinnai and T. P. Russell, *Macromolecules*, 2005, **38**, 10788–10798.
- 25 L. Tsarkova, G. J. A. Sevink and G. Krausch, in *Complex Macromolecular Systems I*, ed. A. H. E. Müller and H.-W. Schmidt, Springer-Verlag, Berlin Heidelberg, 2010, pp. 33–73.
- 26 We note that also so-called non-destructive 3D imaging techniques could damage sensitive materials like thin polymer films (see text). The term “non-destructive” reflects here the fact that the specimen still exists after 3D characterization and does concern quality of the gained sample structures.
- 27 J. Chen, C. Y. Wu, J. P. Tian, W. J. Li, S. H. Yu and Y. C. Tian, *Appl. Phys. Lett.*, 2008, **92**, 233104.
- 28 W. S. Haddad, I. McNulty, J. E. Trebes, E. H. Anderson, R. A. Levesque and L. Yang, *Science*, 1994, **266**, 1213–1215.
- 29 A. P. Hitchcock, G. A. Johansson, G. E. Mitchell, M. H. Keefe and T. Tyliczak, *Appl. Phys. A: Mater. Sci. Process.*, 2008, **92**, 447–452.
- 30 C. R. Parkinson and A. Sasov, *Dent. Mater.*, 2008, **24**, 773–777.
- 31 J. Petrasch, P. Wyss, R. Stampfli and A. Steinfeld, *J. Am. Ceram. Soc.*, 2008, **91**, 2659–2665.
- 32 L. C. Sawyer and D. T. Grubb, *Polymer Microscopy*, Chapman & Hall, London, 1996.
- 33 H. Jinnai, Y. Nishikawa, R. J. Spontak, S. D. Smith, D. A. Agard and T. Hashimoto, *Phys. Rev. Lett.*, 2000, **84**, 518–521.
- 34 P. A. Midgley and M. Weyland, *Ultramicroscopy*, 2003, **96**, 413–431.
- 35 L. H. Radzilowski, B. O. Carragher and S. I. Stupp, *Macromolecules*, 1997, **30**, 2110–2119.
- 36 M. K. Miller, *Atom Probe Tomography: Analysis at the Atomic level*, Kluwer Academic/Plenum Publishers, New York, 2000.
- 37 D. N. Dunn and R. Hull, *Appl. Phys. Lett.*, 1999, **75**, 3414–3416.
- 38 L. Holzer, B. Muench, M. Wegmann, P. Gasser and R. J. Flatt, *J. Am. Ceram. Soc.*, 2006, **89**, 2577–2585.
- 39 B. Tomiyasu, I. Fukuju, H. Komatsubara, M. Owari and Y. Nihei, *Nucl. Instrum. Methods Phys. Res., Sect. B*, 1998, **137**, 1028–1033.
- 40 T. S. Yeoh, J. A. Chaney, M. S. Leung, N. A. Ives, Z. D. Feinberg, J. G. Ho and J. U. Wen, *J. Appl. Phys.*, 2007, **102**, 123104.
- 41 E. C. Spitzner, C. Riesch and R. Magerle, *ACS Nano*, 2011, **5**, 315–320.
- 42 A. E. Efimov, A. G. Tonevitsky, M. Dittrich and N. B. Matsko, *J. Microsc.*, 2007, **226**, 207–217.
- 43 W. Denk and H. Horstmann, *PLoS Biol.*, 2004, **2**, 1900–1909.
- 44 C. Harrison, M. Park, P. M. Chaikin, R. A. Register, D. H. Adamson and N. Yao, *Polymer*, 1998, **39**, 2733–2744.
- 45 C. Harrison, M. Park, P. M. Chaikin, R. A. Register, D. H. Adamson and N. Yao, *Macromolecules*, 1998, **31**, 2185–2189.
- 46 M. Göken, R. Magerle, M. Hund and K. Durst, in *Fortschritte in der Metallographie*, ed. P. D. Portella, Werkstoffinformationsgesellschaft mbH, Frankfurt, 2003, pp. 257–262.
- 47 M. Konrad, A. Knoll, G. Krausch and R. Magerle, *Macromolecules*, 2000, **33**, 5518–5523.
- 48 R. Magerle, *Phys. Rev. Lett.*, 2000, **85**, 2749–2752.
- 49 C. Dietz, S. Roper, S. Scherdel, A. Bernstein, N. Rehse and R. Magerle, *Rev. Sci. Instrum.*, 2007, **78**, 053703.
- 50 C. Dietz, M. Zerson, C. Riesch, A. M. Giggler, R. W. Stark, N. Rehse and R. Magerle, *Appl. Phys. Lett.*, 2008, **92**, 143107.
- 51 B. Pittenger, *HarmoniX™ Microscopy for Materials Characterization*, Veeco application note AN112, Rev. A0, courtesy of Bruker AXS.
- 52 O. Sahin, S. Magonov, C. Su, C. F. Quate and O. Solgaard, *Nat. Nanotechnol.*, 2007, **2**, 507–514.
- 53 B. Pittenger, N. Erina and C. Su, *Quantitative Mechanical Property Mapping at the Nanoscale with PeakForce QNM*, Veeco application note AN128, Rev. A0, courtesy of Bruker AXS.
- 54 C. M. Chan, T. M. Ko and H. Hiraoka, *Surf. Sci. Rep.*, 1996, **24**, 3–54.
- 55 F. S. Denes and S. Manolache, *Prog. Polym. Sci.*, 2004, **29**, 815–885.
- 56 S. Ludwigs, K. Schmidt, C. M. Stafford, E. J. Amis, M. J. Fasolka, A. Karim, R. Magerle and G. Krausch, *Macromolecules*, 2005, **38**, 1850–1858.
- 57 H. G. Schoberth, V. Olszowka, K. Schmidt and A. Böker, in *Complex Macromolecular Systems I*, ed. A. H. E. Müller and H.-W. Schmidt, Springer-Verlag, Berlin Heidelberg, 2010, pp. 1–31.
- 58 M. Hund and H. Herold, *Ger. Pat.*, 10 2004 043 191 B4, 24th May 2006 and *US Pat.*, 7,934,417, 3rd May 2011.
- 59 M. Hund and H. Herold, *Rev. Sci. Instrum.*, 2007, **78**, 063703.
- 60 A. Sperschneider, M. Hund, H. G. Schoberth, F. H. Schacher, L. Tsarkova, A. H. E. Müller and A. Böker, *ACS Nano*, 2010, **4**, 5609–5616.
- 61 M. Hund, V. Olszowka, H. Krejtschi and F. Fischer, *Patent Application Publication* DE 10 2010 015 966 A1, 15 Sept. 2011.
- 62 S. Ludwigs, A. Böker, V. Abetz, A. H. E. Müller and G. Krausch, *Polymer*, 2003, **44**, 6815–6823.
- 63 S. Ludwigs, G. Krausch, R. Magerle, A. V. Zvelindovsky and G. J. A. Sevink, *Macromolecules*, 2005, **38**, 1859–1867.
- 64 N. Rehse, A. Knoll, R. Magerle and G. Krausch, *Macromolecules*, 2003, **36**, 3261–3271.
- 65 V. Olszowka, V. Kuntermann and A. Böker, *Macromolecules*, 2008, **41**, 5515–5518.
- 66 V. Olszowka, PhD thesis, Universität Bayreuth, Germany, 2007.
- 67 S. Ludwigs, A. Böker, A. Voronov, N. Rehse, R. Magerle and G. Krausch, *Nat. Mater.*, 2003, **2**, 744–747.
- 68 S. Ludwigs, K. Schmidt and G. Krausch, *Macromolecules*, 2005, **38**, 2376–2382.
- 69 H. Elbs, PhD thesis, Universität Bayreuth, Germany, 2001.
- 70 N. Grassie and G. Scott, *Polymer Degradation and Stabilisation*, Cambridge University Press, Cambridge, 1988.
- 71 A. Knoll, K. S. Lyakhova, A. Horvat, G. Krausch, G. J. A. Sevink, A. V. Zvelindovsky and R. Magerle, *Nat. Mater.*, 2004, **3**, 886–890.
- 72 D. Q. Ly, T. Honda, T. Kawakatsu and A. V. Zvelindovsky, *Soft Matter*, 2009, **5**, 4814–4822.
- 73 H. Elbs, K. Fukunaga, R. Stadler, G. Sauer, R. Magerle and G. Krausch, *Macromolecules*, 1999, **32**, 1204–1211.
- 74 A. Horvat, G. J. A. Sevink, A. V. Zvelindovsky, A. Krekhov and L. Tsarkova, *ACS Nano*, 2008, **2**, 1143–1152.
- 75 L. Tsarkova, A. Horvat, G. Krausch, A. V. Zvelindovsky, G. J. A. Sevink and R. Magerle, *Langmuir*, 2006, **22**, 8089–8095.
- 76 K. S. Lyakhova, G. J. A. Sevink, A. V. Zvelindovsky, A. Horvat and R. Magerle, *J. Chem. Phys.*, 2004, **120**, 1127–1137.
- 77 L. Tsarkova, A. Knoll, G. Krausch and R. Magerle, *Macromolecules*, 2006, **39**, 3608–3615.
- 78 A. Knoll, PhD thesis, Universität Bayreuth, Germany, 2003.
- 79 A. Horvat, K. S. Lyakhova, G. J. A. Sevink, A. V. Zvelindovsky and R. Magerle, *J. Chem. Phys.*, 2004, **120**, 1117–1126.
- 80 K. Schmidt, A. Böker, H. Zettl, F. Schubert, H. Hänsel, F. Fischer, T. M. Weiss, V. Abetz, A. V. Zvelindovsky, G. J. A. Sevink and G. Krausch, *Langmuir*, 2005, **21**, 11974–11980.